

Spitzer Observations of M83 and the Hot Star, H II Region Connection

Robert H. Rubin^{1,2}, Janet P. Simpson^{1,3}, Sean W.J. Colgan¹, Reginald J. Dufour⁴, Katherine L. Ray¹, Edwin F. Erickson¹, Michael R. Haas¹, Adalbert W.A. Paudlach⁵, and Robert I. Citron¹

rubin@cygnus.arc.nasa.gov; simpson@cygnus.arc.nasa.gov

September 23, 2018

ABSTRACT

We have undertaken a program to observe emission lines of [S IV] 10.51, [Ne II] 12.81, [Ne III] 15.56, and [S III] 18.71 μm in a number of extragalactic H II regions with the Spitzer Space Telescope. Here we report our results for the nearly face-on spiral galaxy M83. A subsequent paper will present our data and analysis for another substantially face-on spiral galaxy M33. The nebulae selected cover a wide range of galactocentric radii (R_G). The observations were made with the Infrared Spectrograph in the short wavelength, high dispersion configuration. The above set of four lines is observed cospatially, thus permitting a reliable comparison of the fluxes. From the measured fluxes, we determine the ionic abundance ratios including $\text{Ne}^{++}/\text{Ne}^+$, $\text{S}^{3+}/\text{S}^{++}$, and $\text{S}^{++}/\text{Ne}^+$ and find that there is a correlation of increasingly higher ionization with larger R_G . By sampling the dominant ionization states of Ne and S for H II regions, we can approximate the Ne/S ratio by $(\text{Ne}^+ + \text{Ne}^{++})/(\text{S}^{++} + \text{S}^{3+})$. Our findings of ratios that significantly exceed the benchmark Orion Nebula value, as well as a decrease in this ratio with increasing R_G , are more likely due to other effects than a true gradient in Ne/S. Two effects that will tend to lower these high estimates and to flatten the gradient are first, the method does not account for the presence of S^+ and second, S but not Ne is incorporated into grains. Both

¹NASA/Ames Research Center, Moffett Field, CA 94035-1000, USA

²Orion Enterprises, M.S. 245-6, Moffett Field, CA 94035-1000, USA

³SETI Institute, 515 N. Whisman Road, Mountain View, CA 94043, USA

⁴Physics & Astronomy Department, Rice University, MS 61, Houston, TX 77005-1892, USA

⁵University of Munich, Munich D-81679, Germany

Ne and S are primary elements produced in α -chain reactions, following C and O burning in stars, making their yields depend very little on the stellar metallicity. Thus, it is expected that Ne/S remains relatively constant throughout a galaxy. We stress that this type of observation and method of analysis does have the potential for accurate measurements of Ne/S, particularly for H II regions that have lower metallicity and higher ionization than those here, such as those in M33. Our observations may also be used to test the predicted ionizing spectral energy distribution (SED) of various stellar atmosphere models. We compare the ratio of fractional ionizations $\langle \text{Ne}^{++} \rangle / \langle \text{S}^{++} \rangle$ and $\langle \text{Ne}^{++} \rangle / \langle \text{S}^{3+} \rangle$ vs. $\langle \text{S}^{3+} \rangle / \langle \text{S}^{++} \rangle$ with predictions made from our photoionization models using several of the state-of-the-art stellar atmosphere model grids. The overall best fit appears to be the nebular models using the supergiant stellar atmosphere models of Pauldrach et al. (2001) and Sternberg, Hoffmann, & Pauldrach (2003). This result is not sensitive to the electron density and temperature range expected for these M83 nebulae. Considerable computational effort has gone into the comparison between data and models, although not all parameter studies have yet been performed on an ultimate level (e.g., in the present paper the stellar atmosphere model abundances have been fixed to solar values). A future paper, with the benefit of more observational data, will continue these studies to further discriminate how the ionic ratios depend on the SED and the other nebular parameters.

Subject headings: ISM: abundances, H II regions, stars: atmospheres, galaxies: individual (M83)

1. Introduction

Most observational studies of the chemical evolution of the universe rest on emission line objects, which define the mix of elemental abundances at advanced stages of evolution as well as the current state of the interstellar medium (ISM). Gaseous nebulae are laboratories for understanding physical processes in all emission-line sources and probes for stellar, galactic, and primordial nucleosynthesis. H II regions are also among the best tracers of recent star formation.

The presence of radial (metal/H) abundance gradients in the plane of the Milky Way is well established in both gaseous nebulae and stars (e.g., Henry & Worthey 1999; Rolleston et al. 2000). Radial abundance gradients seem to be ubiquitous in spiral galaxies, though the degree varies depending on a given spiral’s morphology and luminosity class.

The gradients are generally attributed to the radial dependence of star formation history and ISM mixing processes (e.g., Shields 2002). Thus, the observed gradients are a major tool for understanding galactic evolution (e.g., Hou et al. 2000; Chiappini et al. 2001; Chiappini et al. 2003). The premise is that star formation and chemical enrichment begins in the nuclear bulges of the galaxies and subsequently progresses outward into the disk, which has remained gas-rich. The higher molecular gas density in the inner regions produces a higher star formation rate, which results in a relatively greater return to the ISM of both “primary” α -elements (including O, Ne, and S) from massive star supernovae, and “secondary” elements like N. Secondary nitrogen is produced by CNO burning of already existing carbon and oxygen in intermediate-mass stars and is subsequently returned to the ISM through mass loss. However, because chemical evolution models have uncertain input parameters, and because details of the abundance variations of each element are uncertain, current understanding of the formation and evolution of galaxies suffers (e.g., Pagel 2001).

Studies of H II regions in the Milky Way are hampered by interstellar extinction. For the most part, optical studies (e.g., Shaver et al. 1983) have been limited to those H II regions at galactocentric radius $R_G \gtrsim 6$ kpc (predicated on $R_\odot = 8$ kpc) because H II regions are very concentrated to the Galactic plane. Here extinction becomes severe with increasing distance from Earth. Observations using far-infrared (FIR) emission lines have penetrated the $R_G \lesssim 6$ kpc barrier. Surveys with the Kuiper Airborne Observatory (KAO) by Simpson et al. (1995), Afferbach et al. (1997), and Rudolph et al. (2006) have observed 16 inner Galaxy H II regions. With the Infrared Space Observatory (ISO), Martín-Hernández et al. (2002a) observed 13 inner Galaxy H II regions covering FIR and also mid-IR lines. A major finding of these studies is that inner Galaxy H II regions generally have lower excitation (ionization) compared to those at larger R_G . This holds for both heavy element ionic ratios O^{++}/S^{++} (Simpson et al. 1995) and Ne^{++}/Ne^+ (Simpson & Rubin 1990; Giveon et al. 2002), and also He^+/H^+ measured from radio recombination lines (Churchwell et al. 1978; Thum, Mezger, & Pankonin 1980). Whether the observed increase in excitation with increasing R_G comes entirely from heavy element opacity effects in the H II regions and stellar atmospheres, or also from a gradient in the maximum stellar effective temperature, T_{eff} , of the exciting stars is still a point of controversy (e.g., Giveon et al. 2002; Martín-Hernández et al. 2002b; Smith, Norris, & Crowther 2002; Morisset et al. 2004).

It has become clear that nebular plasma simulations with photoionization modeling codes are enormously sensitive to the ionizing spectral energy distribution (SED) that is input (e.g., Simpson et al. 2004, and references therein). These SEDs need to come from stellar atmosphere models. Stellar atmosphere modelers are paying increasing attention to the usefulness of nebular observations, particularly of H II regions, in validating and constraining their models (e.g., Stasińska & Schaerer 1997). Though it may be somewhat

chauvinistic to say so, much of this increased attention stems from work we did pointing out the “[Ne III] problem” and possible solutions (Simpson et al. 1995; Rubin et al. 1995; Sellmaier et al. 1996). To produce Ne^{++} requires ionizing photons > 41 eV. At energies exceeding this ionization potential (IP), modern stellar atmosphere model SEDs are especially divergent. A critical test of the validity of stellar atmosphere models of hot stars is whether H II region models produced with these atmospheres predict line fluxes that agree with observations. The “[Ne III] problem” is that the observed $\text{Ne}^{++}/\text{O}^{++}$ ratio significantly exceeds model predictions and remains relatively constant over a large range of H II region excitation as gauged by the $\text{O}^{++}/\text{S}^{++}$ ratio. The original observational basis is KAO FIR measurements of [Ne III] 36, [O III] 52, and [S III] 33 μm lines in Galactic H II regions (see figure 3 in Simpson et al. 1995).

While Sellmaier et al. (1996) believed that they had solved the [Ne III] problem when they obtained a good fit to the FIR data by using non-LTE atmospheres with winds computed with Pauldrach’s code as it then existed, we recently investigated the problem and concluded that it still exists (Simpson et al. 2004). Our H II region models using non-LTE stellar atmospheres with winds from Pauldrach, Hoffmann, & Lennon (2001) and from atmosphere models by both Smith et al. (2002) and Sternberg, Hoffmann, & Pauldrach (2003) using Pauldrach’s WM-BASIC code predict much lower $\text{Ne}^{++}/\text{O}^{++}$ than observed for “Dwarf” atmospheres with $T_{\text{eff}} < 40,000$ K and for “Supergiant” atmospheres with $T_{\text{eff}} < 35,000$ K. Moreover, the models without winds do a poorer job of reproducing the observations than those that include winds.

In this paper, we develop new observational tests of and constraints on the ionizing SEDs that are predicted from various stellar atmosphere models. We do this by utilizing Spitzer Space Telescope (SST) observations of H II regions in the spiral galaxy M83. M83 (NGC 5236) is one of the closest (distance 3.7 Mpc) and brightest spirals (SBc II), as well as being nearly face-on ($i = 24^\circ$) (de Vaucouleurs et al. 1983). M83 particularly interested us because of its high metallicity (at least twice solar, e.g., Dufour et al. 1980; Bresolin & Kennicutt 2002). High metallicity should correlate with lower-ionization H II regions. From our experience with the [Ne III] problem, this is likely to provide the most stringent test matching theory with observations. With the Infrared Spectrograph (IRS) on the SST, we can observe four emission lines that probe the dominant ionization states of neon and sulfur in these H II regions. These lines are: [Ne II] 12.81, [Ne III] 15.56, [S III] 18.71, and [S IV] 10.51 μm . Crucially, SST permits the **simultaneous, cospacial** observation of these four lines.

We discuss the SST/IRS observations in section 2. In section 3, the data are used to test for a variation in the degree of ionization of the H II regions with R_G . We examine

the Ne/S abundance ratio for our M83 H II region sample in section 4. Section 5 describes how these Spitzer data are used to constrain and test the ionizing SEDs predicted by stellar atmosphere models. Last, we provide a summary and conclusions in section 6.

2. Spitzer Space Telescope Observations

In the nearly face-on (tilt 24°) spiral galaxy M83, we observed 24 H II regions, covering a wide range of deprojected galactocentric radii (R_G). We used the SST/IRS in the short wavelength, high dispersion (spectral resolution ~ 600) configuration, called the short-high (SH) mode (e.g., Houck et al. 2004). This covers the wavelength range from 9.9 – 19.6 μm permitting cospatial observations of all four of our program emission lines: [S IV] 10.51, [Ne II] 12.81, [Ne III] 15.56, and [S III] 18.71 μm . The SH bandpass also covers the hydrogen $\text{H}\alpha$, also called H(7–6), at 12.37 μm . Unfortunately, we were not able to detect this line in any of the 24 H II regions observed.

The observations were made in 2005, February and July. Figure 1 shows the regions and apertures observed, while Table 1 lists the H II region positions and the aperture grid configuration used to observe it. Nebulae with RK and deV designations are from Rumstoy & Kaufman (1983) and de Vaucouleurs et al. (1983), respectively. The size of the SH aperture is 11.3'' \times 4.7''. In all cases, we chose the mapping mode with aperture grid patterns varying from a 1 \times 2 grid to as large as a 2 \times 4 grid in order to cover the bulk of the emission. Maps were arranged with the apertures immediately abutting each other; that is, with no overlap or space between them. In order to save overhead time, we clustered the objects into “Astronomical Observing Templates” (AOTs) with the same aperture grid pattern.

Our data were processed and calibrated with both versions S12.0.2 and S13.2.0 of the standard IRS pipeline at the Spitzer Science Center (SSC). For each position, we have 16 cycles with 30 sec ramp duration. The basic calibrated data (bcd images) for each telescope pointing were median-combined and cleaned of rogue pixels and noisy order edges (the ends of the slit). The spectra were extracted and the lines measured using the IRS Spectroscopic Modeling, Analysis and Reduction Tool (SMART, Higdon et al. 2004). For the brighter lines, we find little change in the line fluxes between the two pipeline versions. Generally the [S IV] 10.5 line was weakest; for these we used the later version of the pipeline. The emission lines were measured with SMART using a Gaussian line fit. The continuum baseline was fit with a linear or quadratic function. Figures 2 (a)–(d) show the fits for each of the four lines in RK209 (object #9 in Fig. 1). A line is deemed to be detected if the flux is at least as large as the 3σ uncertainty. We measure the uncertainty by the product of the FWHM and the root-mean-square variations in the adjacent, line-free continuum; it does not include

systematic effects.

We now discuss and estimate systematic uncertainties for our specific case using IRS in SH mode. Most likely the largest uncertainty is due to slit (aperture) loss factors. The pipeline flux calibration assumes that objects are point sources. Our nebulae are extended and that is why we mapped each with a grid that covers more than a single aperture. We did not make a correction for this effect. Thus we have implicitly assumed that the H II regions are close to the point-source limit within the SH $11.3'' \times 4.7''$ aperture. If the H II region were uniformly extended within the SH aperture, correction factors would need to be applied to our fluxes. These are: 0.697, 0.663, 0.601, and 0.543 for the 10.5, 12.8, 15.6, and 18.7 μm lines respectively (Simpson et al. in preparation). These factors were obtained by interpolating in numbers provided from the *b1_slitloss_convert.tbl* file from the Spitzer IRS Custom Extraction tool (SPICE) for the SH module (see <http://ssc.spitzer.caltech.edu/postbcd/spice.html>). For the uniformly filled aperture, the maximum uncertainty in the flux due to this effect would be $\sim 46\%$ for the [S III] 18.7 line. The correction factors would need to multiply our listed fluxes. We note that with regard to this effect, the fluxes listed in Table 2 are upper limits and that the uncertainty would be in only the direction to lower them. No correction factor was applied because we are likely closer to the point-source limit than the uniform-brightness limit. Because our science depends on line flux ratios, for our purposes, the possible uncertainty due to this effect would be lower, e.g., $\sim 22\%$ when we deal with the line flux ratio [S IV] 10.5/[S III] 18.7.

According to §7.2 *Spectroscopic Flux Calibration Uncertainties* (Infrared Spectrograph Data Handbook, ver. 2.0 (<http://ssc.spitzer.caltech.edu/irs/dhb>)), the minimum uncertainty possible in the absolute flux calibration of the spectroscopic products delivered by the pipeline is $\pm 5\%$ due to the “photometric uncertainty introduced by uncertainty in the angular sizes of the standard stars and their spectral types”. It is also stated that the maximum uncertainty [for a point source] is $\pm 10\%$ by comparisons with other Spitzer instruments.

Any uncertainty in the flux due to a pointing error is probably small and in the worst case should not exceed 10%. We arrive at this estimate as follows. The absolute pointing accuracy of Spitzer is $\sim 1''$ rms. Since a spectral map is performed by alignment of a guide star, this is effectively the pointing uncertainty for each spatial position in the spectral map. Because our smallest map dimensions are $11.3'' \times 9.4''$, an error of $1''$ could result in an error of $\sim 10\%$ if the source uniformly filled the map area and went to zero outside of it.

For the brighter lines, i.e., most of the 12.8, 15.6, and 18.7 μm lines, the systematic uncertainty far exceeds the measured (statistical) uncertainty. Even for the fainter lines, we estimate that the systematic uncertainty exceeds the measured uncertainty.

In addition to the line flux, the measured FWHM and radial velocity (V_r) are listed in Table 2. Both the FWHM and V_r are useful in judging the reliability of the line measurements. The FWHM is expected to be the instrumental width for all our lines. With a resolving power for the SH module of ~ 600 , our lines should have a FWHM of roughly 500 km s^{-1} . The values for V_r should straddle the heliocentric systemic radial velocity for M83 of $\sim 516 \text{ km s}^{-1}$ (Lawrence et al. 1999). We note that the IRS pipeline does not correct to heliocentric radial velocities (V_{helio}). At the low ecliptic latitude of M83, the correction of V_r to V_{helio} can be almost $\pm 30 \text{ km s}^{-1}$. It is interesting (but not pertinent) that we can definitely measure an average velocity differential between our February and July data of roughly 60 km s^{-1} , as expected.

3. Variation in the degree of ionization of the H II regions with R_G

From the measured fluxes, we estimate ionic abundance ratios, including $\text{Ne}^{++}/\text{Ne}^+$, $\text{S}^{3+}/\text{S}^{++}$, and $\text{S}^{++}/\text{Ne}^+$, for each of the H II regions. Important advantages compared with prior optical studies of various other ionic ratios are: 1) the IR lines have a weak and similar electron temperature (T_e) dependence while the collisionally-excited optical lines vary exponentially with T_e , and 2) the IR lines suffer far less from interstellar extinction. Indeed for our purposes, the differential extinction correction is negligible as the lines are relatively close in wavelength. In our analysis, we deal with ionic abundance ratios and therefore line flux ratios. In order to derive the ionic abundance ratios, we perform the usual semiempirical analysis assuming a constant T_e and electron density (N_e) to obtain the volume emissivities for the four pertinent transitions. We use the atomic data described in Simpson et al. (2004) and Simpson et al. (in preparation) for the ions Ne^+ , Ne^{++} , S^{++} , and S^{3+} . For the entries in Table 3, we adopt a typical value for all the M83 H II regions of $T_e = 8000 \text{ K}$ and $N_e = 100 \text{ cm}^{-3}$. The H II regions in M83 are known to have a high metallicity (e.g., at least twice solar, Dufour et al. 1980; Bresolin & Kennicutt 2002); thus a value of 8000 K is not unreasonable. This is also typical of the values found for seven H II regions in M83 (see Tables 10 and 11 in Bresolin et al. 2005). Because of the insensitivity of the volume emissivities to T_e , particularly when working with ratios for these IR lines, our results depend very little on this T_e choice. The effects on our analysis due to a change in the assumed N_e are also small as will be discussed later.

We chose our sample of nebulae in order to cover a wide range in R_G . It is a straightforward geometry exercise to derive the deprojected galactocentric distances. This involves knowing the inclination angle ($i = 24^\circ$), position angle of the line of nodes ($\theta = 43^\circ$), and distance ($D = 3.7 \text{ Mpc}$) (de Vaucouleurs et al. 1983). We assumed the centre of the galaxy is

at $\alpha, \delta = 13^{\text{h}}37^{\text{m}}00\overset{\text{s}}{.}92, -29^{\circ}51'56\overset{\text{s}}{.}7$ (J2000) (source NASA/IPAC Extragalactic Database). Table 3 lists R_G for the centre of each object. These range from 0.46 to 5.16 kpc.

We present the variation of $\text{Ne}^{++}/\text{Ne}^+$ with R_G in Figure 3 using the values from Table 3. The error values represent the propagated flux measurement uncertainties and do not include the systematic uncertainties. There is extremely little change in any of these ratios even when using an N_e of 1000 cm^{-3} , which is likely a reasonable upper limit for these H II regions (see Figure 9 in Bresolin et al. 2005). A linear least-squares fit indicates a positive correlation with R_G (in kpc),

$$\text{Ne}^{++}/\text{Ne}^+ = 0.033 \pm 0.010 + (0.011 \pm 0.0035) R_G,$$

with minuscule change to this equation for $N_e = 1000 \text{ cm}^{-3}$. For all the least-squares line fits in this paper, each point is given equal weight because systematic uncertainties exceed the flux measurement uncertainties, as discussed earlier. The positive correlation of $\text{Ne}^{++}/\text{Ne}^+$ with R_G as measured by the slope may be judged to be significant following the criterion that it exceeds the 3σ uncertainty.

A similar fit to the $\text{S}^{3+}/\text{S}^{++}$ vs. R_G data yields

$$\text{S}^{3+}/\text{S}^{++} = -0.00079 \pm 0.0079 + (0.0067 \pm 0.0027) R_G.$$

There is more scatter in the plot (not shown) because the data for the [S IV] 10.5 line are noisier than for the other stronger lines (see Figure 2). The slope exceeds the 1σ uncertainty by a factor of only 2.4. Thus the increase in degree of ionization with increasing R_G in this case would be deemed marginal. We note that one of the points (for RK268) stands out as far above any of the others. If we refit eliminating this far outlier, then

$$\text{S}^{3+}/\text{S}^{++} = 0.0055 \pm 0.0032 + (0.0029 \pm 0.0011) R_G.$$

The slope is not as steep and as 2.5σ would again be deemed marginally significant.

Figure 4 plots the fractional ionic abundance ratio $\langle \text{S}^{++} \rangle / \langle \text{Ne}^+ \rangle$ vs. R_G . This ratio is obtained from the $\text{S}^{++}/\text{Ne}^+$ ratio by multiplying by an assumed Ne/S value (see below). The last three columns of Table 3 list this and other fractional ionic abundance ratios used in this paper. In Figure 4, the filled circles represent the points, and the solid line, the linear least-squares fit for an assumed N_e of 100 cm^{-3} . For H II regions in M83 this is likely the typical N_e value. Here, the fit indicates a significant positive correlation with R_G ,

$$\langle \text{S}^{++} \rangle / \langle \text{Ne}^+ \rangle = 0.43 \pm 0.026 + (0.035 \pm 0.0089) R_G,$$

where angular brackets denote fractional ionization. The lower dashed line is the least-squares fit to points marked with an X derived assuming $N_e = 1000 \text{ cm}^{-3}$. This shows the

effect of higher N_e on the volume emissivity of the [S III] line. The least-squares fit for this density is

$$\langle S^{++} \rangle / \langle Ne^+ \rangle = 0.36 \pm 0.022 + (0.030 \pm 0.0076) R_G,$$

and here too, the slope is statistically significant. In this figure and in these linear fits, we assume an Orion Nebula Ne/S abundance ratio of 14.3 (Simpson et al. 2004). Because Ne and S are “primary” elements, their production is expected to vary in lockstep and Ne/S would not be expected to show a radial gradient within a galaxy (Pagel & Edmunds 1981). There is a clear correlation of increasingly higher ionization with increasing R_G . This is most likely due to the lower metallicity at larger R_G causing the exciting stars to have a harder ionizing spectrum. The first quantitative abundance study of radial gradients for H II regions in M83 found $d\log(O/H)/dR(kpc) = -0.09 \pm 0.02$ dex kpc^{-1} based on differential photoionization modeling (Dufour et al. 1980). With ~ 25 more years of observations, this gradient still appears but has flattened considerably. In their Figure 7, Bresolin & Kennicutt (2002) plot the O/H gradient. When we convert their units to $R(kpc)$ using the M83 distance of 3.7 Mpc, we find $d\log(O/H)/dR(kpc) = -0.0257$ dex kpc^{-1} . A shallower slope is also indicated in Figure 15 (see also their Figure 20) in Bresolin et al. (2005), where the M83 H II region points are shown as open squares. In their Figure 15, M83 has the flattest O/H gradient among the 5 galaxies plotted. Because M83 has a bar, this tends to correlate with a flatter radial abundance gradient (e.g., Martin & Roy 1994) due to radial mixing.

4. Neon to Sulfur abundance ratio

For H II regions, we may approximate the Ne/S ratio with $(Ne^+ + Ne^{++})/(S^{++} + S^{3+})$. This includes the dominant ionization states of these two elements. However this relation does not account for S^+ , which should be present at some level. We may safely ignore the negligible contributions of neutral Ne and S in the ionized region. Figure 5 shows our approximation for Ne/S vs. R_G . There appears to be a drop in the Ne/S ratio with increasing R_G . The expected increasing fraction of S^+ towards the inner galaxy regions would lead to a flatter gradient. Another factor that could flatten the slope is the higher dust content (with S, but not Ne, entering grains) expected in the inner regions due to higher metallicity as is the case for the Milky Way. The refractory carbonaceous and silicate grains are not distributed uniformly throughout the Galaxy but instead increase in density toward the centre. A simple model suggests the dust density is $\sim 5 - 35$ times higher in the inner parts of the Galaxy than in the local ISM (Sandford, Pendleton, & Allamandola 1995). The Ne/S abundance ratios that we derive here are considerably higher than the Orion Nebula value of 14.3 (Simpson et al. 2004). We suspect that all our Ne/S estimates are upper limits because

of the two effects (not accounting for S^+ or dust) with the outer regions likely needing less of a downward correction to obtain a true Ne/S ratio.

The premise that these estimates of Ne/S are upper limits is further supported by our forthcoming work with H II regions in M33. This is a similar study for which we have Spitzer Cycle 2 spectra of roughly 25 nebulae in the substantially face-on spiral M33. A preliminary report was presented at IAU Symposium 235 (Rubin et al. 2006). The Ne/S values (under the same approximation) fell mostly in the range from $\sim 12 - 21$. M33 H II regions have a lower metallicity than those in M83. Also, most of the H II regions we observed in M33 have significantly higher ionization than those we observed in M83. These two facts tend to mitigate the amount of any downward correction needed to account for S^+ and dust. While there appears to be a decrease in our (approximate) Ne/S vs. R_G for M33, our data also indicate that the lower envelope to Ne/S is well fit by a constant value equal to the Orion Nebula ratio (Rubin et al. 2006 and in preparation).

5. Constraints on the ionizing SED for the stars exciting the H II regions

Various fractional ionic abundances are highly sensitivity to the stellar ionizing SED that apply to H II regions. This has been realized, for example, for the $Ne^+ - Ne^{++}$ ionization equilibrium and the total number of photons more energetic than the 41 eV Ne^+ ionization potential that are predicted by various stellar atmosphere models (e.g., Simpson et al. 2004 and references therein). The present Spitzer data probe the Ne^+ and Ne^{++} fractional ionic abundances, as well as those of S^{++} and S^{3+} ; thus they may be used to provide further constraints and tests on the ionizing SED for the stars exciting these M83 nebulae. We use the ratio of fractional ionizations $\langle Ne^{++} \rangle / \langle S^{++} \rangle$ vs. $\langle S^{3+} \rangle / \langle S^{++} \rangle$ (Figure 6a) and $\langle Ne^{++} \rangle / \langle S^{3+} \rangle$ vs. $\langle S^{3+} \rangle / \langle S^{++} \rangle$ (Figure 6b). These ionic ratios are computed using our photoionization code NEBULA (e.g., Simpson et al. 2004; Rodríguez & Rubin 2005). The lines connect the results of the nebular models calculated using the ionizing SEDs predicted from various stellar atmosphere models. There are no other changes to the input parameters, just the SED. The stellar atmospheres used are representative of several recent non-LTE models that apply for O-stars. We also display the results from one set of LTE models by Kurucz (1992). His LTE atmospheres have been extensively used in the past as input for H II region models; hence the comparison with the other non-LTE results reinforces the fact that more reliable SEDs for O-stars require a non-LTE treatment. Figures 6a and b dramatically illustrate how sensitive H II region model predictions of these ionic abundance ratios are to the ionizing SED input to nebular plasma simulations.

For the H II region models calculated with Pauldrach et al. (2001) atmospheres, the

solid line connects models with dwarf atmospheres and the dashed line connects models with supergiant atmospheres. The Sternberg et al. (2003) paper also uses Pauldrach's WM-BASIC code. At a given T_{eff} we have used their model with the smallest $\log g$ in order to be closest to the supergiant case. Because the locus using these Sternberg et al. atmosphere models is for the most part similar to the Pauldrach et al. supergiant locus, we do not show it in Figures 6 to avoid clutter. For H II region models calculated with Lanz & Hubeny (2003) atmospheres (TLUSTY code), the solid line connects models with atmospheres with $\log g = 4.0$ and the dotted and dashed lines connect models with atmospheres with $\log g = 3.0$ to 3.5, and with Lyman continuum luminosities of 10^{49} and 10^{50} photons s^{-1} , respectively. The lines with open squares in Figures 6 are the results of our nebular models with the atmospheres in Martins et al. (2005) that use Hillier's CMFGEN code.

To compare our data with the models, we need to divide the observed $\text{Ne}^{++}/\text{S}^{++}$ and $\text{Ne}^{++}/\text{S}^{3+}$ ratios by an assumed Ne/S abundance ratio. For the purposes of Figure 6, we adopt a constant $\text{Ne}/\text{S} = 14.3$, the Orion Nebula value (Simpson et al. 2004). As per the discussion in §4, we cannot conclude definitively whether Ne/S may vary. The open circles (adjusted by the assumed Ne/S) are derived from our observed line fluxes using N_e of 100 cm^{-3} . The M83 data usually lie closest to the Pauldrach et al. supergiant loci. In addition the points derived from our data as well as those for the H II regions we observed in M33 (Rubin et al. 2006 and in preparation), which are generally of higher ionization, follow the trend of these theoretical loci. This is particularly notable in Figure 6b, where the other model loci are nearly perpendicular to the data point trend in the vicinity of where they intersect the data points.

The nebular models used to generate Figures 6 are all constant density, spherical models. We used a constant total nucleon density (DENS) of 1000 cm^{-3} that begins at the star. Each model used a total number of Lyman continuum photons s^{-1} (N_{LyC}) = 10^{49} . The same *nebular* elemental abundance set was used for all nebular models. We use the same "reference" set as in Simpson et al. (2004) because in that paper we were studying the effects of various SEDs on other ionic ratios and other data sets. Ten elements are included with their abundance by number relative to H as follows: (He, C, N, O, Ne, Si, S, Ar, Fe) with (0.100, 3.75E-4, 1.02E-4, 6.00E-4, 1.50E-4, 2.25E-5, 1.05E-5, 3.75E-6, 4.05E-6), respectively. While the purpose here was not to try to match the abundances in the H II regions we observed in M83, the set of abundances used is roughly a factor of 1.5 higher than for Orion and not drastically different from solar. We have investigated the effects of changing DENS, N_{LyC} , and allowing for a central evacuated cavity, characterized by an initial radius (R_{init}) before the stellar radiation encounters nebular material. We term these shell models. In Figures 7a and 7b, the resulting changes to Figures 6a and 6b are shown for six nebular models run using two of the Pauldrach et al. (2001) supergiant atmospheres. These are listed along

with the symbol:

- (1) $T_{\text{eff}} = 35000$ K; DENS = 1000 cm^{-3} ; $R_{\text{init}} = 0.5 \text{ pc}$; $N_{LyC} = 10^{49} \text{ s}^{-1}$ (asterisk)
- (2) $T_{\text{eff}} = 35000$ K; DENS = 100 cm^{-3} ; $R_{\text{init}} = 0 \text{ pc}$; $N_{LyC} = 10^{49} \text{ s}^{-1}$ (triangle)
- (3) $T_{\text{eff}} = 35000$ K; DENS = 100 cm^{-3} ; $R_{\text{init}} = 0 \text{ pc}$; $N_{LyC} = 10^{50} \text{ s}^{-1}$ (X)
- (4) $T_{\text{eff}} = 40000$ K; DENS = 1000 cm^{-3} ; $R_{\text{init}} = 0.5 \text{ pc}$; $N_{LyC} = 10^{49} \text{ s}^{-1}$ (asterisk)
- (5) $T_{\text{eff}} = 40000$ K; DENS = 100 cm^{-3} ; $R_{\text{init}} = 0 \text{ pc}$; $N_{LyC} = 10^{49} \text{ s}^{-1}$ (triangle)
- (6) $T_{\text{eff}} = 40000$ K; DENS = 100 cm^{-3} ; $R_{\text{init}} = 0 \text{ pc}$; $N_{LyC} = 10^{50} \text{ s}^{-1}$ (X)

The original Pauldrach et al. (2001) supergiant locus and points derived from the Spitzer data are shown again. We also display the effects of using a different N_e to interpret our line measurements in terms of ionic ratios. The open stars show the results with N_e of 1000 cm^{-3} while the original points (open circles) were derived with $N_e = 100 \text{ cm}^{-3}$. The change is slight with the higher N_e shifting points to the upper right in Figure 7a and to the lower right in Figure 7b.

The points for cases (3) and (6) are nearly identical to the original points for the Pauldrach supergiant models at the same respective T_{eff} . This can be understood in terms of the ionization parameter (U), which is very useful for gauging ionization structure. An increase in U corresponds to higher ionization (for a given T_{eff}). For an ionization bounded, constant density case,

$$U = [N_e N_{LyC} (\alpha - \alpha_1)^2 / (36\pi c^3)]^{1/3},$$

where $(\alpha - \alpha_1)$ is the recombination rate coefficient to excited levels of hydrogen, and c is the velocity of light (see Rubin et al. 1994, eq. 1 and adjoining discussion). Because $(\alpha - \alpha_1) \simeq 4.10 \times 10^{-10} T_e^{-0.8} \text{ cm}^3 \text{ s}^{-1}$ (Rubin 1968 fit to Seaton 1959), there is only a weak dependence of U on T_e ($\sim T_e^{-0.5}$). When U is similar, as is the case here with the product of $N_e \times N_{LyC}$, the ionization structure is similar. With regard to the two shell models in Figures 7, the Strömgren radius is $\sim 0.74 \text{ pc}$. Thus the radial thickness of the shell is slightly less than half the radius of the central cavity. From the visual appearance of our target H II regions, it is unlikely that the theoretical loci need to be tracked to higher dilutions.

Another *nebular* parameter that can alter the theoretical tracks is the set of elemental abundances used. This is certainly well established. For instance, in the grid of model H II regions of Rubin (1985), the fractional ionic abundances needed here were tabulated considering a variation in the heavy-element abundance set of a factor of 10. The up (“U”) and down (“D”) sets in that paper were meant to represent $\sqrt{10}$ and $1/\sqrt{10}$ times the nebular (“N”) Orion-like abundances at that time. A sampling of those models, that are closest to

the parameter space of interest in this paper, indicates median shifts of the following factors: $\langle \text{Ne}^{++} \rangle / \langle \text{S}^{++} \rangle = 3.50$, $\langle \text{Ne}^{++} \rangle / \langle \text{S}^{3+} \rangle = 1.39$, and $\langle \text{S}^{3+} \rangle / \langle \text{S}^{++} \rangle = 2.13$, when going from “U” to “D” sets. Much more apropos for the current situation, we have calculated two variants of the Pauldrach $T_{\text{eff}} = 40000$ K supergiant (canonical model in Figures 6 and 7) with the only change being in the *nebular* abundance set by scaling all the heavy elements by a factor of two higher and two lower than the set used for all other models. This is more than sufficient to cover the expected variation in our M83 sample allowing for the heavy-element gradient $d\log(\text{O/H})/dR(\text{kpc}) = -0.0257$ dex kpc^{-1} (see §3). As expected, lower metallicity results in a shift to higher ionization. In both Figures 6a,b, the point moves to the upper right; the factors are $\langle \text{Ne}^{++} \rangle / \langle \text{S}^{++} \rangle = 1.29$, $\langle \text{Ne}^{++} \rangle / \langle \text{S}^{3+} \rangle = 1.16$, and $\langle \text{S}^{3+} \rangle / \langle \text{S}^{++} \rangle = 1.11$. Likewise, higher metallicity shifts the point to the lower left. This latter change is relatively larger with factors: $\langle \text{Ne}^{++} \rangle / \langle \text{S}^{++} \rangle = 1.62$, $\langle \text{Ne}^{++} \rangle / \langle \text{S}^{3+} \rangle = 1.26$, and $\langle \text{S}^{3+} \rangle / \langle \text{S}^{++} \rangle = 1.28$. In the case of the M83 nebulae, we may conclude that the predicted spread in Figures 6 due to a reasonable uncertainty in nebular metallicity is far less than that due to the SEDs of the various stellar atmosphere models.

There is also the effect of a change in the abundances used to compute the stellar atmosphere models. This will change the emergent stellar SED (e.g., Mokiem et al. 2004). As is the case for a change in the nebular model abundance set, such a modification in the stellar model will alter the shape of the SED in the same sense; that is, a higher metallicity will cause more opacity and soften the SED, and a lower metallicity will do the opposite. Mokiem et al. (2004) examined this using CMFGEN stellar models matching both the nebular and stellar metallicities. Their Figure 11 tracks the predicted variation in the $[\text{Ne III}] 15.6 / [\text{Ne II}] 12.8$ flux ratio over a range of $0.1 - 2 Z_{\odot}$.

Although beyond the scope of this paper, it would be interesting to compare models using different stellar atmosphere metallicities, especially if the environment indicates significant departures from solar. However, presently the proper abundances are not accurately known and comparisons like those presented in this paper will help decipher the proper values. Improvements with regard to this point are deferred for a future paper, where the curves for different metallicities are compared with the observations. With the present paper, however, we have been investigating which of the models best fits the observations and such a comparison works most effectively with a fixed set of abundances *common to all models*, which are the solar ones.

Such additional degrees of freedom (besides the SED) in the nebular models makes judging how well a particular stellar atmosphere model set fits observations more challenging. We will revisit these fits in a second paper that has the benefit of additional observational data of H II regions in M33 (Rubin et al. in preparation).

6. Summary and conclusions

We have observed emission lines of [Ne II] 12.81, [Ne III] 15.56, [S III] 18.71, and [S IV] 10.51 μm cospatially with the Spitzer Space Telescope using the Infrared Spectrograph (IRS) in short-high mode (SH). From the measured fluxes, we determined the ionic abundance ratios $\text{Ne}^{++}/\text{Ne}^+$, $\text{S}^{3+}/\text{S}^{++}$, and $\text{S}^{++}/\text{Ne}^+$ in 24 H II regions in the substantially face-on spiral galaxy M83. These nebulae cover a range from 0.46 to 5.16 kpc in deprojected galactocentric distance R_G . We found a correlation of increasingly higher ionization with increasing R_G . This is seen in the variation of $\text{Ne}^{++}/\text{Ne}^+$ and $\langle \text{S}^{++} \rangle / \langle \text{Ne}^+ \rangle$ with R_G (see Figures 3 and 4). This is most likely due to the lower metallicity at larger R_G causing the exciting stars to have a harder ionizing spectrum.

By sampling the dominant ionization states of Ne and S for H II regions, we can approximate the Ne/S ratio by $(\text{Ne}^+ + \text{Ne}^{++})/(\text{S}^{++} + \text{S}^{3+})$. The decrease in this ratio with increasing R_G is more likely due to other effects than a true gradient in Ne/S. Both Ne and S are the products of α -chain reactions following carbon and oxygen burning in stars, with large production factors from core-collapse supernovae. Both are primary elements, making their yields depend very little on the stellar metallicity. Thus, at least to “first order”, it is expected that Ne/S remains relatively constant throughout a galaxy.

As discussed in §4, our estimate for Ne/S has not accounted for the presence of S^+ . Because inner-galaxy H II regions have lower ionization (§3), it is possible that there would be a larger fractional ionization of S^+ towards the inner galaxy regions and hence a flatter Ne/S slope than indicated in Figure 5. A second factor which might flatten this apparent gradient is the higher grain content in the inner regions due to higher metallicity. All of our derived Ne/S abundance ratios are considerably higher than the benchmark Orion Nebula value of 14.3. Because we did not account for S^+ or dust (with the objects at larger R_G likely needing less of a downward correction to obtain a true Ne/S ratio), our Ne/S estimates may be considered upper limits. This conclusion is further supported by our subsequent work on H II regions in M33 where this methodology leads to lower estimates for Ne/S. This was briefly discussed in §4 with citations to a conference proceedings and a future paper (Rubin et al. 2006 and in press). Thus with observations of the set of four IR emission lines and the analysis we have described, there is the potential for reliable Ne/S measurements, especially for H II regions that have lower metallicity and higher ionization than those in M83.

At the present time, the solar abundance, particularly of Ne, is the subject of much controversy (e.g., Drake & Testa 2005; Bahcall, Serenelli, & Basu 2006; and references in each of these). While we cannot directly address the solar abundance with our observations of extragalactic H II regions, it is important to have reliable benchmarks for the neon

abundance. There appears to be a growing body of evidence that the Ne abundance [its fractional number abundance relative to hydrogen $\log H = 12$, by definition and termed $A(H)$] is substantially higher in the solar neighborhood, and even in the Sun itself, than the “canonical” solar values given in two recent, often-referenced papers. These papers have for the Sun: $A(\text{Ne}) = 7.87$, $A(\text{S}) = 7.19$ (Lodders 2003) and $A(\text{Ne}) = 7.84$, $A(\text{S}) = 7.14$ (Asplund, Grevesse, & Sauval 2005). Thus $\text{Ne}/\text{S} \sim 5$ according to both. It is now generally accepted that Ne has the least well determined solar abundance among the most abundant elements. One of the proponents for a higher Ne abundance pointed out that an $A(\text{Ne}) = 8.29$ would reconcile solar models with the helioseismological measurements (Bahcall, Basu, & Serenelli 2005). Using this value together with the $A(\text{S})$ values above, we obtain Ne/S of 12.6 and 14.1, respectively, close to the Orion Nebula ratio (Simpson et al. 2004).

According to calculations based on the theoretical nucleosynthesis, galactic chemical evolution models of Timmes, Woosley, & Weaver (1995), the Ne/S ratio in the solar neighborhood would change little, from 3.80 to 3.75, between solar birth and the present time (apropos for the Orion Nebula). These calculations were provided by Frank Timmes (private communication). With regard to these ratios being even lower than the canonical solar values, Timmes notes that although massive stars are expected to dominate the Ne and S production (and are all that were included in their non-rotating models with no wind losses), there is likely to be some re-distribution of Ne and S from rotation or from Wolf-Rayet phases of evolution, along with contributions of Ne from novae or even heavier intermediate mass stars. Hence, the theoretical model Ne/S ratios above should be a lower bound because some potential sources of Ne are missing.

Additionally, the data here may be used as constraints on the ionizing SEDs for the stars exciting these nebulae by comparing the ratio of fractional ionizations $\langle \text{Ne}^{++} \rangle / \langle \text{S}^{++} \rangle$ and $\langle \text{Ne}^{++} \rangle / \langle \text{S}^{3+} \rangle$ vs. $\langle \text{S}^{3+} \rangle / \langle \text{S}^{++} \rangle$ with predictions made from our photoionization models using stellar atmosphere models from several different sources. Figures 6 show the comparison, where we assume that the Ne/S ratio does not vary and equals the Orion Nebula value. Generally, the best fit is to the nebular models using the supergiant stellar atmosphere models (Pauldrach et al. 2001) computed with the WM-BASIC code. We note that this comparison is mainly qualitative since these ionic ratios depend not only on the SED, but also on the nebular parameters discussed as well as the effects of the stellar metallicity on the SED. This result is not sensitive to the electron density range, 100 and 1000 cm^{-3} , expected for these M83 nebulae. Furthermore, the points derived from our M83 data, as well as those for the H II regions we observed in M33 (Rubin et al. 2006 and in preparation), which are generally of higher ionization, follow the trend of the above-mentioned theoretical loci. In fact, the other model loci are nearly perpendicular to the data point trend in the vicinity of where they intersect the data points in Figure 6b. We reiterate that we do not infer that

the actual exciting stars are supergiants, but only that their SEDs have similar shape as the supergiant atmospheres computed using WM-BASIC.

It is possible that a plot similar to Figures 6a,b using $\langle \text{Ne}^{++} \rangle / \langle \text{Ne}^+ \rangle$ for the ordinate will also have utility in comparing data with models using different SEDs. While the $\langle \text{Ne}^{++} \rangle / \langle \text{Ne}^+ \rangle$ ratio has the advantage of being independent of elemental abundance ratios, it appears to be more sensitive to the *nebular* parameters than does the $\langle \text{Ne}^{++} \rangle / \langle \text{S}^{3+} \rangle$ ratio. This fact tends to make it less unique in its ability to discriminate between the stellar SEDs we present in this paper. We defer this investigation until our next paper that has the addition of more Spitzer data with H II regions in M33.

This work is based on observations made with the Spitzer Space Telescope, which is operated by the Jet Propulsion Laboratory, California Institute of Technology under NASA contract 1407. Support for this work was provided by NASA for this Spitzer program identification 3412. RHR had further support from the NASA Long-Term Space Astrophysics (LTSA) program. We thank Frank Timmes for providing information on the Ne/S ratio from a nucleosynthesis, galactic chemical evolution perspective. We thank Brendan Wakefield and Danny Key for assistance with the data reduction. Valuable comments by the referee are much appreciated. The nebular models were run on a Cray computer at JPL. Funding for its use in this investigation was provided by the JPL Office of the Chief Information Officer.

REFERENCES

Afflerbach A., Churchwell E., Werner M.W., 1997, ApJ, 478, 190

Asplund M., Grevesse N., Sauval A.J., 2005, in Cosmic Abundances as Records of Stellar Evolution and Nucleosynthesis, ed. T.G. Barnes III, F.N. Bash, ASP Conf. Ser., 336, 25

Bahcall J.N., Basu S., Serenelli A.M., 2005, ApJ, 631, 1281

Bahcall J.N., Serenelli A.M., Basu S., 2006, ApJS, 165, 400

Bresolin F., Kennicutt R.C. Jr., 2002, ApJ, 572, 838

Bresolin F., Schaerer D., González Delgado R.M., Stasińska G., 2005, A&A, 441, 981

Chiappini C., Matteucci F., Romano D., 2001, ApJ, 554, 1044

Chiappini C., Romano D., Matteucci F., 2003, MNRAS, 339, 63

Churchwell E., Smith L.F., Mathis J., Mezger P.G., Huchtmeier W., 1978, A&A, 70, 719

de Vaucouleurs G., Pence W.D., Davoust E., 1983, ApJS, 53, 17

Drake J.J., Testa P., 2005, Nature, 436, 525

Dufour R.J., Talbot R.J. Jr., Jensen E.B., Shields G.A., 1980, ApJ, 236, 119

Giveon U., Sternberg A., Lutz D., Feuchtgruber H., Pauldrach A.W.A., 2002, ApJ, 566, 880

Henry R.B.C., Worthey G., 1999, PASP, 111, 919

Higdon S.J.U., et al., 2004, PASP, 116, 975

Hou J.L., Prantzos N., Boissier S., 2000, A&A, 362, 921

Houck J.R., et al., 2004, ApJS, 154, 18

Kurucz R.L., 1992, in IAU Symp. 149, Stellar Population of Galaxies, ed. B. Barbuy A. Renzini, p. 225

Lanz T., Hubeny I., 2003, ApJS, 146, 417

Lawrence A., Rowan-Robinson M., Ellis R.S., Frenk C.S., Efstathiou G., Kaiser N., Saunders W., Parry I.R., Xiaoyang Xia, Crawford J., 1999, MNRAS, 308, 897

Lodders K., 2003, ApJ, 591, 1220

Martin P., Roy J.-R., 1994, ApJ, 424, 599

Martín-Hernández N.L., et al., 2002a, A&A, 381, 606

Martín-Hernández N.L., Vermeij R., Tielens A.G.G.M., van der Hulst J.M., Peeters E., 2002b, A&A, 389, 286

Martins F., Schaerer D., Hillier D.J., 2005, A&A, 436, 1049

Mokiem M.R., Martín-Hernández N.L., Lenorzer A., de Koter A., Tielens A.G.G.M., 2004, A&A, 419, 319

Morisset C., Schaerer D., Bouret J.-C., Martins F., 2004, A&A, 415, 577

Pagel B.E.J., 2001, PASP, 113, 137

Pagel B.E.J., Edmunds, M.G., 1981, ARA&A, 19, 77

Pauldrach A.W.A., Hoffmann T.L., Lennon M., 2001, A&A, 375, 161

Rodríguez M., Rubin R.H., 2005, ApJ, 626, 900

Rolleston W.R.J., Smartt S.J., Dufton P.L., Ryans R.S.I., 2000, A&A, 363, 537

Rubin R.H., 1968, ApJ, 154, 391

Rubin R.H., 1985, ApJS, 57, 349

Rubin R.H., Kunze D., Yamamoto T., 1995, *Astrophys. Appl. of Powerful New Atomic Databases*, A.S.P. Conf. Ser. 78, p.479

Rubin R.H., Simpson J.P., Colgan S.W.J., Dufour R.J., Citron R.I., Ray K.L., Erickson E.F., Haas M.R., Pauldrach A.W.A., 2006, in *Galaxy Evolution Across the Hubble Time*, IAU Symposium 235, Eds. F. Combes & J. Palous, (Cambridge U. Press) (in press)

Rubin R.H., Simpson J.P., Lord S.D., Colgan S.W.J., Erickson E.F., Haas M.R., 1994, ApJ, 420, 772

Rudolph A.L., Fich M., Bell G.R., Norsen T., Simpson J.P., Haas M.R., Erickson E.F., 2006, ApJS, 162, 346

Rumstay K.S., Kaufman M., 1983, ApJ, 274, 611

Sandford S.A., Pendleton Y.J., & Allamandola L.J., 1995, ApJ, 440, 697

Seaton M.J., 1959, MNRAS, 119, 81

Sellmaier F., Yamamoto T., Pauldrach A.W.A., Rubin R.H., 1996, A&A, 305, L37

Shaver P.A., McGee R.X., Newton L.M., Danks A.C., Pottasch S.R., 1983, MNRAS, 204, 53

Shields G.A., 2002, RMxAC, 12, 189

Simpson J.P., Colgan S.W.J., Rubin R.H., Erickson E.F., Haas M.R., 1995, ApJ, 444, 721

Simpson J.P., Rubin R.H., 1990, ApJ, 354, 165

Simpson J.P., Rubin R.H., Colgan S.W.J., Erickson E.F., Haas M.R., 2004, ApJ, 611, 338

Smith L.J., Norris R.P.F., Crowther P.A., 2002, MNRAS, 337, 1309

Stasińska G., Schaerer D., 1997, A&A, 322, 615

Sternberg A., Hoffmann T.L., Pauldrach A.W.A., 2003, ApJ, 599, 1333

Thum C., Mezger P.G., Pankonin V., 1980, A&A, 87, 269

Timmes F.X., Woosley S.E., Weaver T.A., 1995, ApJS, 98, 617

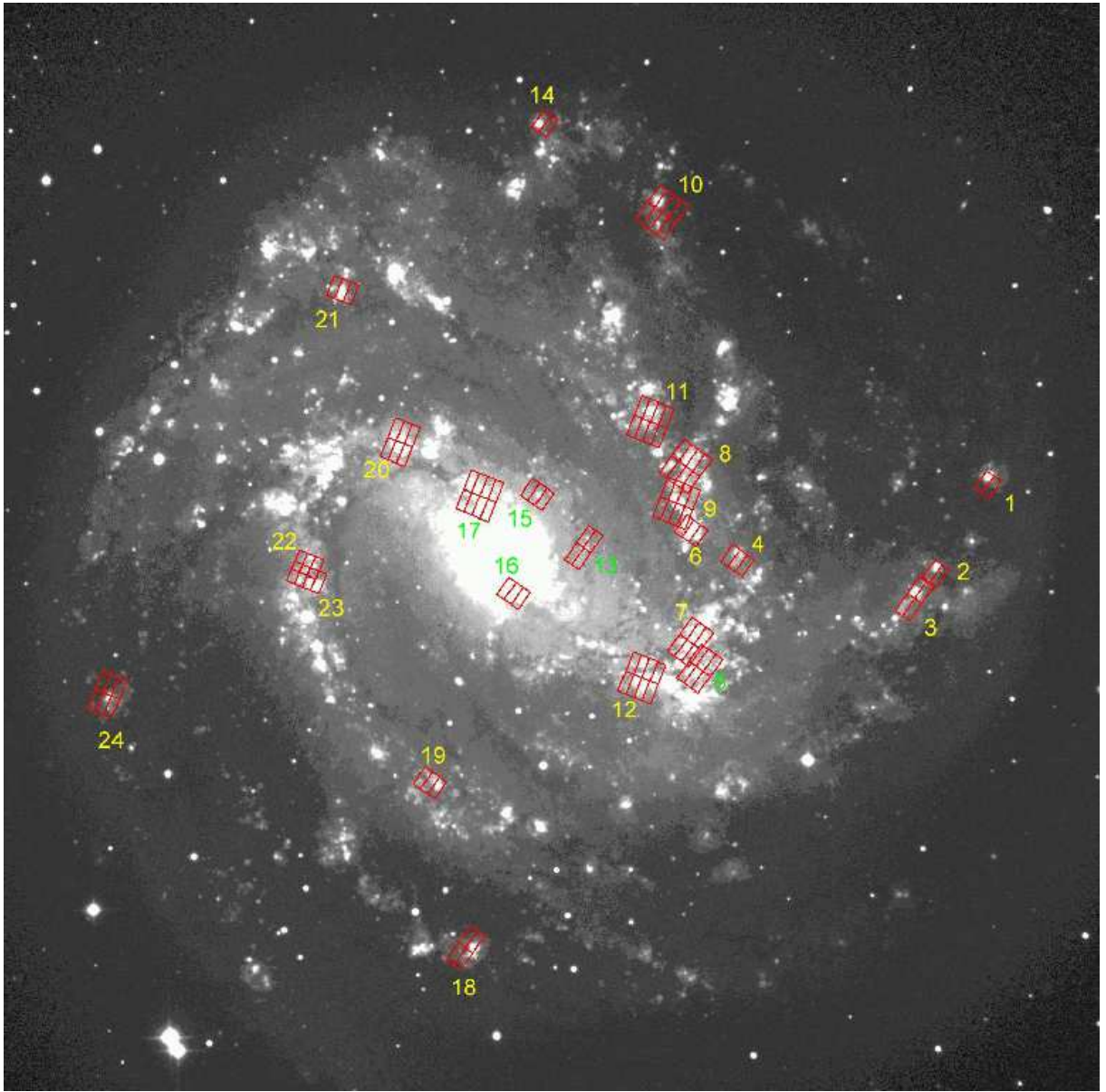


Fig. 1.— The positions and apertures observed for 24 H II regions are shown in red superimposed on an H α image of the nearly face-on (tilt 24°) M83. The nebulae are numbered W to E (see Table 1). N is up and E left.

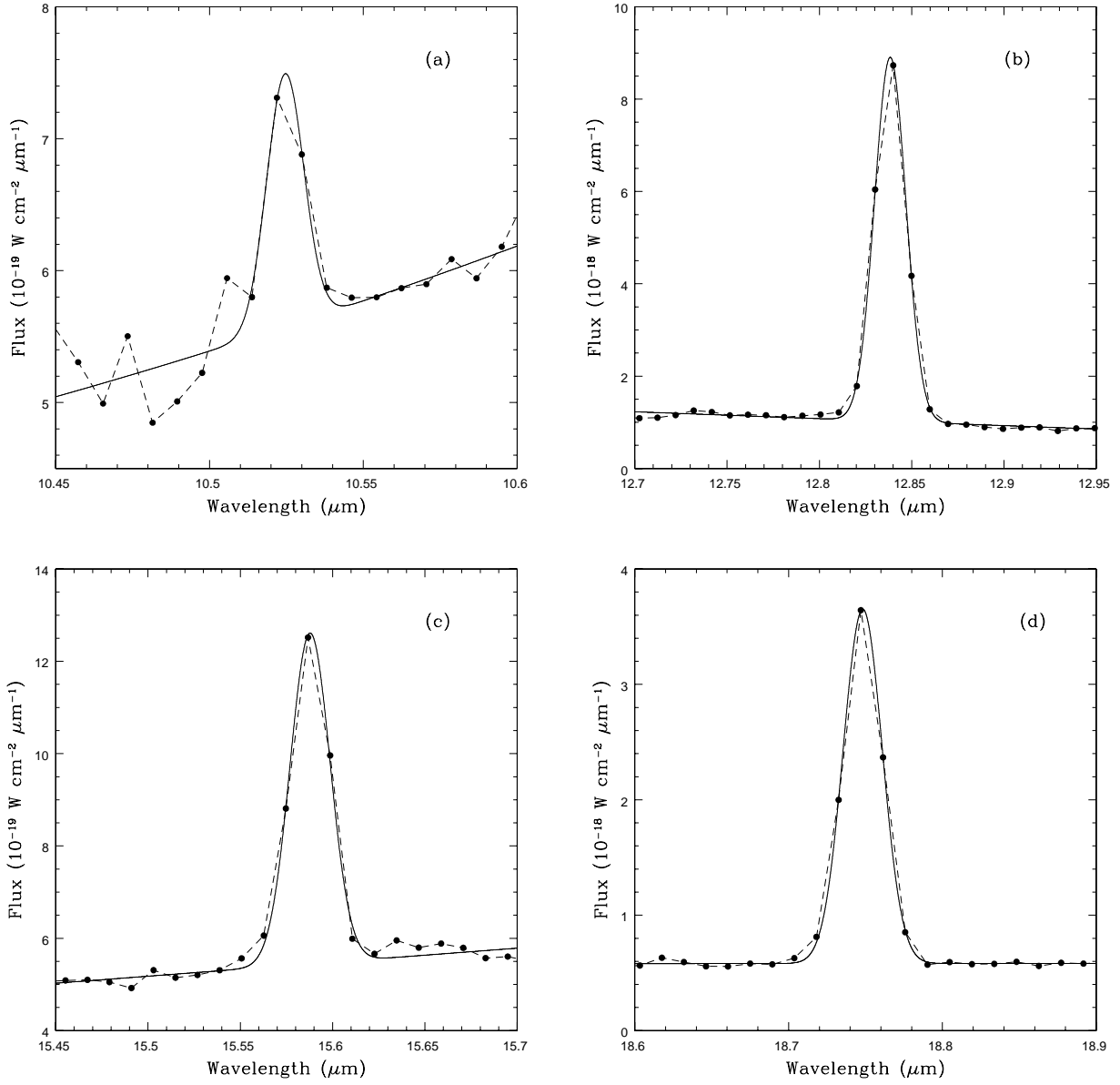


Fig. 2.— Measurements of the four emission lines in the H II region RK209 (#9 in Fig. 1): **(a)** [S IV] 10.5 μm ; **(b)** [Ne II] 12.8 μm ; **(c)** [Ne III] 15.6 μm ; and **(d)** [S III] 18.7 μm . The data points are the filled circles. The fits to the continuum and Gaussian profiles are the solid lines. Such measurements provide the set of line fluxes for further analysis.

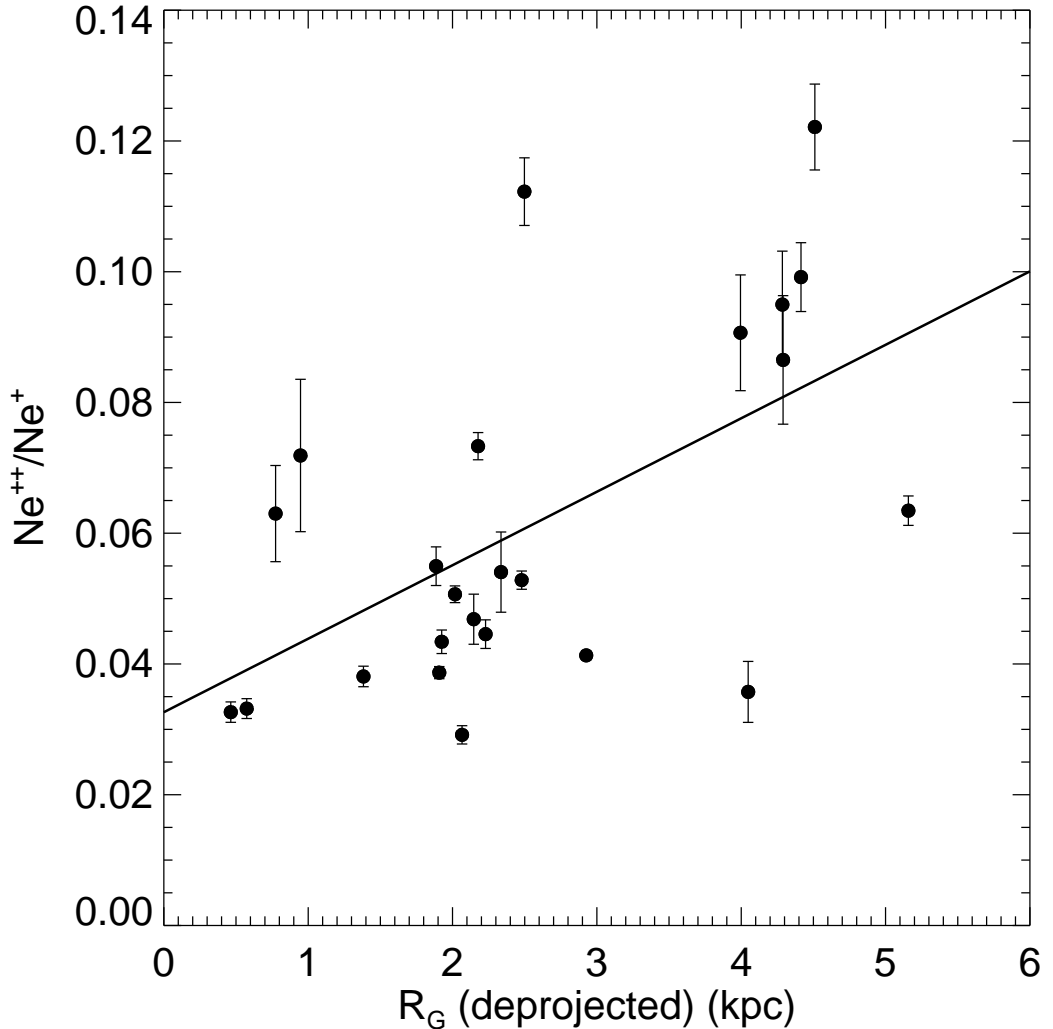


Fig. 3.— Plot of the ionic abundance ratio Ne^{++}/Ne^+ , which is derived from the measured line flux ratios for each H II region, vs. R_G . We assume an electron density (N_e) of 100 cm^{-3} . There is extremely little change with N_e over the range expected for these regions (see text). The linear least-squares fit indicates a positive correlation with R_G . Error bars here and in Figures 4 and 5 are for the propagated measurement uncertainties and do not include the systematic uncertainties (see text).

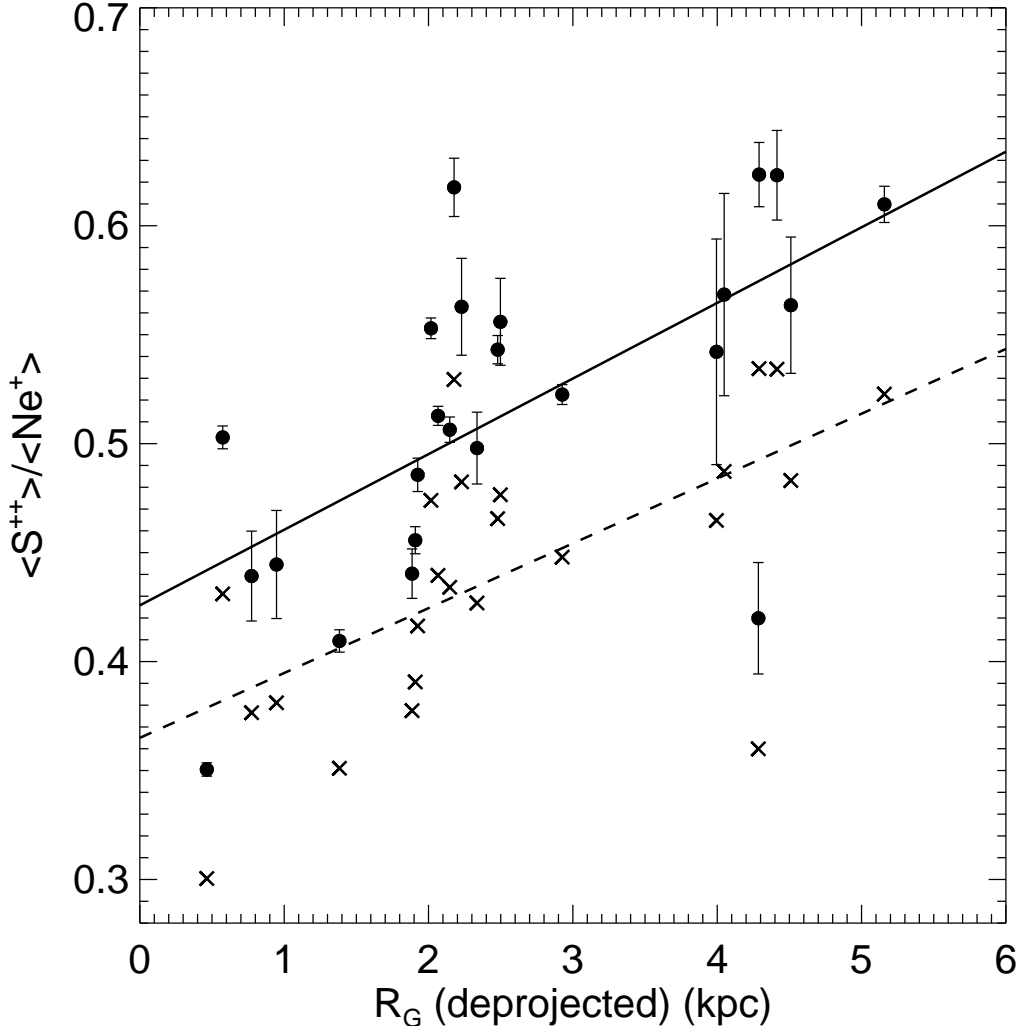


Fig. 4.— Plot showing the fractional ionic abundance ratio $\langle S^{++} \rangle / \langle Ne^+ \rangle$ vs. R_G . Circles represent the points and the solid line the linear least-squares fit for an assumed N_e of 100 cm^{-3} . For H II regions in M83 this is likely the typical N_e value with an upper limit of roughly 1000 cm^{-3} . We plot with an X the points and a dashed line the least-squares fit for an assumed $N_e = 1000 \text{ cm}^{-3}$, thereby showing the effect of higher N_e on the volume emissivity of the [S III] line. The plotted $\langle S^{++} \rangle / \langle Ne^+ \rangle$ ratio assumes an Orion Nebula Ne/S abundance ratio of 14.3 (Simpson et al. 2004). Because Ne and S are “primary” elements, their production is expected to vary in lockstep and Ne/S would not be expected to show a radial gradient within a galaxy (Pagel & Edmunds 1981). There is less scatter about the fit than for the $\langle Ne^{++} \rangle / \langle Ne^+ \rangle$ ratio because the [Ne III] line is weaker than either the [Ne II] or [S III] line in these objects. Error bars are shown for the solid points only to avoid congestion.

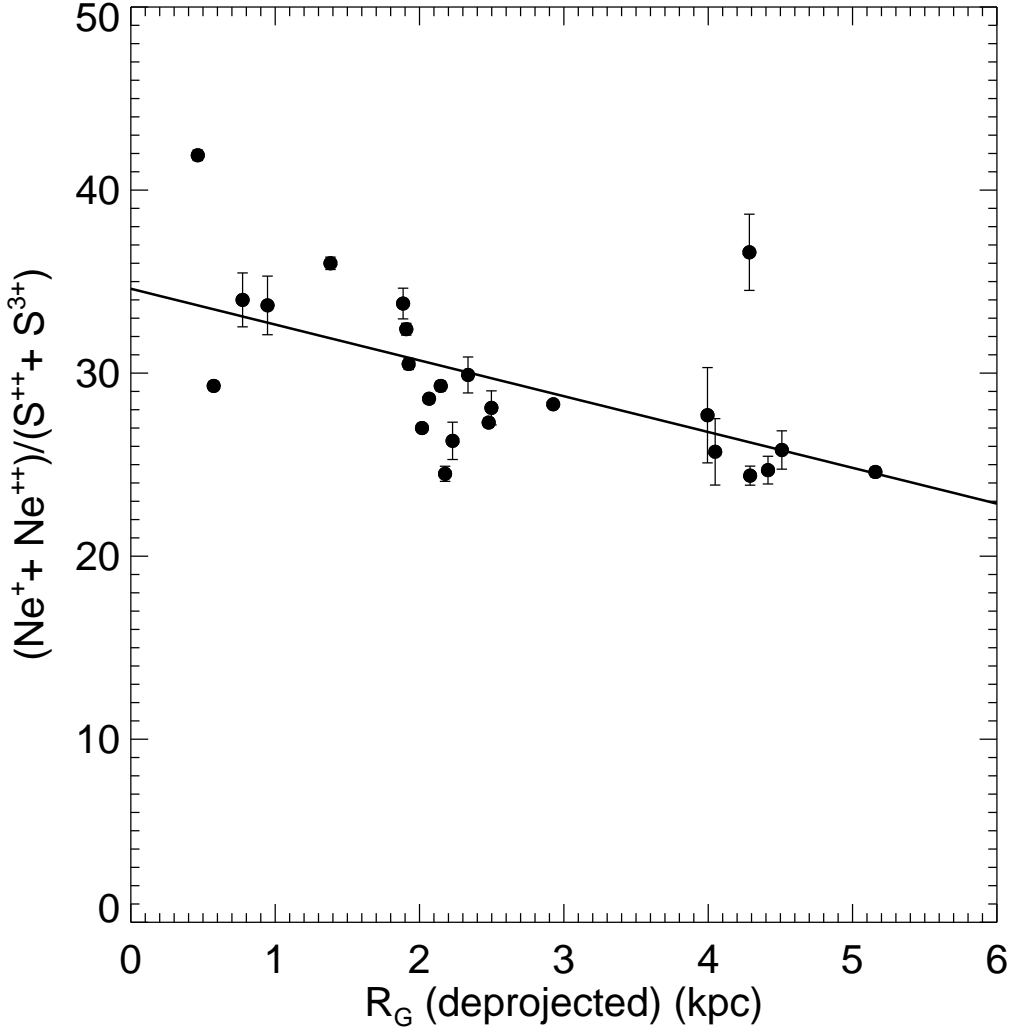


Fig. 5.— Ne/S, as approximated by $(Ne^+ + Ne^{++})/(S^{++} + S^{3+})$ (see text) vs. R_G . These ratios are all larger than the Orion Nebula value of 14.3. There also appears to be a drop in the Ne/S ratio with increasing R_G . However we do not account for S^+ , which must exist in these low ionization M83 H II region. Accounting for S^+ would lower our estimate of Ne/S. The expected increasing fraction of S^+ towards the inner galaxy regions would also lead to a flatter gradient. Another factor that could lower all the derived Ne/S values, as well as flatten the slope, is the higher dust content (with S, but not Ne, entering grains) expected in the inner regions due to higher metallicity.

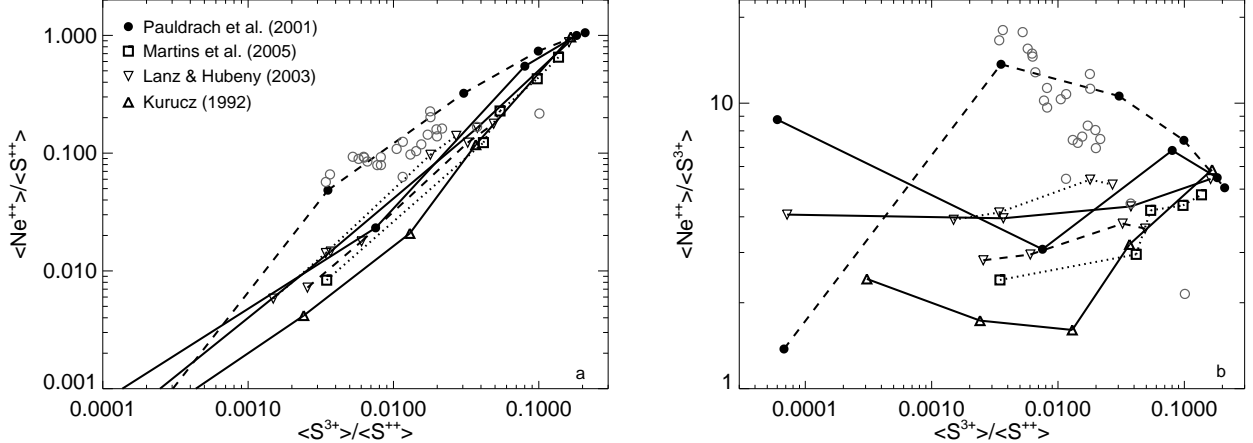


Fig. 6.— a) Theoretical predictions of the fractional ionization ratios $\langle \text{Ne}^{++} \rangle / \langle \text{S}^{++} \rangle$ vs. $\langle \text{S}^{3+} \rangle / \langle \text{S}^{++} \rangle$, computed using our photoionization code NEBULA. The lines connect the results of nebular models calculated with the ionizing SEDs predicted from various stellar atmosphere models as labeled, changing no other parameter except the SED. For the H II region models calculated with Pauldrach et al. (2001) atmospheres, the solid line connects models with dwarf atmospheres and the dashed line connects models with supergiant atmospheres. For the H II region models calculated with Lanz & Hubeny atmospheres, the solid line connects models with atmospheres with $\log g = 4.0$ and the dotted and dashed lines connect models with atmospheres with $\log g = 3.0$ to 3.5, and with Lyman continuum luminosities of 10^{49} and 10^{50} photons s^{-1} , respectively. To compare our data with the models, we need to divide the observed $\text{Ne}^{++}/\text{S}^{++}$ and $\text{Ne}^{++}/\text{S}^{3+}$ ratios by an assumed Ne/S abundance ratio. We use the Orion Nebula $\text{Ne}/\text{S} = 14.3$. The open circles (adjusted by the assumed Ne/S) are derived from our observed line fluxes using N_e of 100 cm^{-3} . b) The same as panel a) except the ordinate is $\langle \text{Ne}^{++} \rangle / \langle \text{S}^{3+} \rangle$. Both panels dramatically illustrate the sensitivity of the H II region model predictions of these ionic abundance ratios to the ionizing SED that is input to nebular plasma simulations. The M83 data, for the most part, appear to lie closest to the Pauldrach et al. supergiant loci.

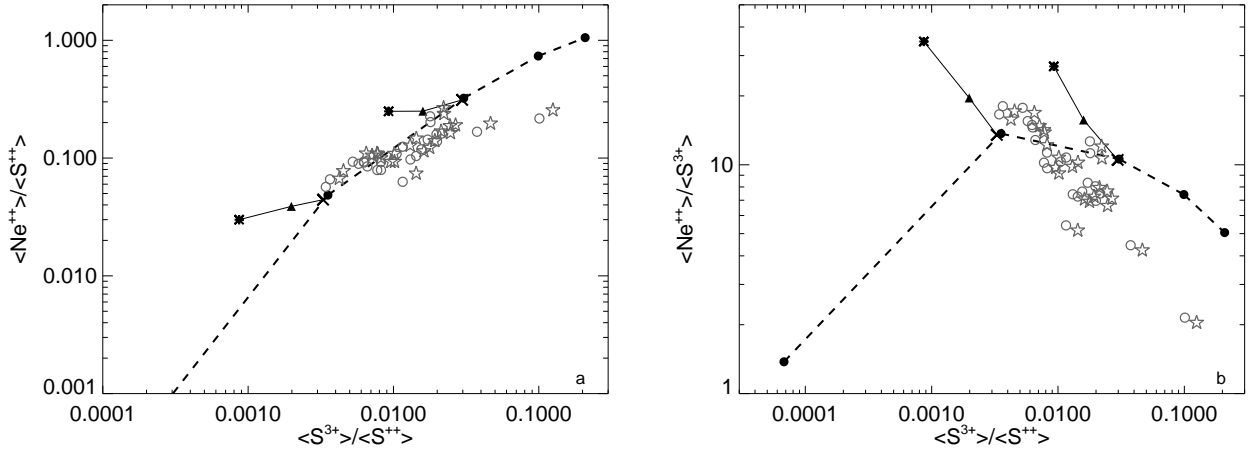


Fig. 7.— **a)** This is similar to Figure 6a. We again show the locus that uses the Pauldrach et al. (2001) supergiant atmospheres. Here we display the results of making some changes to the *nebular parameters* for the $T_{\text{eff}} = 35000$ and 40000 K stellar atmospheres. The points with an * are for a model with a central cavity of radius 0.5 pc (see text); those with a triangle have a density of 100 instead of 1000 cm^{-3} ; and those with an X have a larger number of Lyman continuum photons s^{-1} ($N_{\text{Lyc}} = 10^{50}$ instead of 10^{49}). Points corresponding to the same T_{eff} are connected by the solid lines. Again, the open circles are derived from our observed line fluxes using N_e of 100 cm^{-3} . The open stars show the results of using $N_e = 1000$ cm^{-3} – a slight shift of the points to the upper right. **b)** This is similar to Figure 6b with the same modifications as described for panel a). As shown by the open stars, an $N_e = 1000$ cm^{-3} (compared with $N_e = 100$ cm^{-3}) shifts the points slightly to the lower right.

Table 1. H II Regions Observed in M83

Order	H II Region	RA	J2000	DEC	Aperture Grid
1	RK275	13 36 40.3		-29 51 21	1x2
2	RK268	13 36 42.5		-29 52 09	1x2
3	RK266	13 36 43.4		-29 52 22	2x2
4	RK230	13 36 50.7		-29 52 02	1x3
5	deV10	13 36 52.3		-29 53 00	2x3
6	RK213	13 36 52.6		-29 51 46	1x3
7	deV13	13 36 52.7		-29 52 46	2x3
8	RK211	13 36 52.9		-29 51 11	2x4
9	RK209	13 36 53.2		-29 51 31	2x4
10	RK201	13 36 53.9		-29 48 54	2x4
11	RK198	13 36 54.3		-29 50 47	2x4
12	deV22	13 36 54.7		-29 53 05	2x4
13	RK172	13 36 57.1		-29 51 55	2x2
14	RK154	13 36 58.7		-29 48 06	1x2
15	deV28	13 36 59.0		-29 51 26	1x3
16	deV31	13 37 00.0		-29 52 19	1x3
17	RK137	13 37 01.4		-29 51 27	2x4
18	RK135	13 37 02.0		-29 55 31	2x2
19	RK120	13 37 03.5		-29 54 02	1x3
20	RK110	13 37 04.7		-29 50 58	2x3
21	RK86	13 37 07.1		-29 49 36	1x3
22	RK69	13 37 08.5		-29 52 04	1x3
23	deV52+RK70	13 37 08.6		-29 52 11	1x4
24	RK20	13 37 16.9		-29 53 14	2x3

Table 2. M83 Line Measurements

Order	Source	Line μm	Flux W cm^{-2}	1σ error W cm^{-2}	FWHM km s^{-1}	V_r km s^{-1}
1	RK275	10.5	9.73E-22	1.19E-22	360	454
		12.8	2.25E-20	1.96E-22	510	627
		15.6	3.27E-21	1.12E-22	493	680
		18.7	1.44E-20	1.56E-22	501	610
2	RK268	10.5	1.15E-21	2.16E-22	809	613
		12.8	4.06E-21	1.60E-22	504	651
		15.6	1.14E-21	4.15E-23	456	693
		18.7	2.41E-21	9.71E-23	465	606
3	RK266	10.5	1.62E-21	4.20E-22	711	650
		12.8	2.64E-20	3.12E-22	504	657
		15.6	5.22E-21	5.90E-22	502	690
		18.7	1.73E-20	3.65E-22	496	631
4	RK230	10.5	8.14E-22	1.22E-22	385	417
		12.8	1.65E-20	2.47E-22	526	638
		15.6	4.23E-21	1.84E-22	513	694
		18.7	9.61E-21	3.23E-21	505	629
5	deV10	10.5	2.13E-21	1.22E-22	290	467
		12.8	8.41E-20	6.42E-22	483	674
		15.6	1.02E-20	1.15E-21	517	718
		18.7	4.30E-20	1.43E-21	498	653
6	RK213	10.5	7.40E-22	1.23E-22	392	508
		12.8	8.51E-20	2.78E-22	476	654
		15.6	5.68E-21	2.72E-22	479	697
		18.7	4.59E-20	3.73E-22	487	635
7	deV13	10.5	2.01E-21	2.66E-22	293	461
		12.8	9.80E-20	7.14E-22	472	672
		15.6	1.05E-20	8.54E-22	502	706
		18.7	5.21E-20	4.77E-22	491	648
8	RK211	10.5	2.30E-21	2.25E-22	326	434
		12.8	1.01E-19	1.15E-21	499	624
		15.6	1.03E-20	4.90E-22	529	665
		18.7	5.95E-20	2.32E-21	495	605
9	RK209	10.5	2.90E-21	3.25E-22	404	403
		12.8	1.68E-19	1.04E-21	467	580
		15.6	1.95E-20	4.78E-22	491	631
		18.7	9.77E-20	5.97E-22	478	563
10	RK201	10.5	2.79E-21	4.19E-22	495	434
		12.8	2.76E-20	4.30E-22	484	566
		15.6	5.73E-21	5.53E-22	906	587
		18.7	1.58E-20	1.53E-21	486	567
11	RK198	10.5	3.45E-21	3.99E-22	548	362
		12.8	7.25E-20	1.02E-21	479	549
		15.6	1.22E-20	3.01E-22	516	587
		18.7	4.71E-20	8.02E-22	487	528
12	deV22	10.5	2.99E-21	4.76E-22	716	280

Table 2—Continued

Order	Source	Line μm	Flux W cm ⁻²	1 σ error W cm ⁻²	FWHM km s ⁻¹	V _r km s ⁻¹
13	RK172	12.8	2.00E-19	1.91E-21	490	512
		15.6	1.77E-20	3.91E-22	469	655
		18.7	9.60E-20	9.62E-22	491	595
		10.5	4.67E-22	1.20E-22	343	539
14	RK154	12.8	1.03E-20	3.00E-22	514	605
		15.6	1.57E-21	2.57E-22	431	658
		18.7	4.59E-21	2.21E-22	437	601
		10.5	6.78E-22	9.92E-23	300	385
15	deV28	12.8	1.11E-20	1.50E-22	502	551
		15.6	2.52E-21	1.30E-22	550	570
		18.7	7.29E-21	2.26E-22	506	530
		10.5	5.21E-22	1.51E-22	497	407
16	deV31	12.8	1.39E-20	2.81E-22	488	563
		15.6	2.01E-21	2.31E-22	809	593
		18.7	6.44E-21	2.82E-22	470	560
		10.5	1.04E-21	7.98E-23	294	463
17	RK137	12.8	1.14E-19	6.59E-22	496	621
		15.6	8.49E-21	4.04E-22	542	661
		18.7	4.19E-20	2.84E-22	505	602
		10.5	1.56E-21	3.67E-22	415	342
18	RK135	12.8	1.71E-19	1.09E-21	488	518
		15.6	1.30E-20	5.88E-22	557	570
		18.7	9.05E-20	7.71E-22	493	502
		10.5	7.76E-22	1.15E-22	325	531
19	RK120	12.8	2.38E-20	1.04E-21	495	649
		15.6	1.95E-21	2.40E-22	466	661
		18.7	1.42E-20	1.01E-21	480	629
		10.5	1.99E-21	8.66E-23	439	419
20	RK110	12.8	5.66E-20	4.44E-22	484	604
		15.6	6.84E-21	1.72E-22	474	646
		18.7	3.23E-20	3.00E-22	493	599
		10.5	1.43E-21	3.02E-22	458	379
21	RK86	12.8	1.13E-19	9.78E-22	480	499
		15.6	9.85E-21	3.98E-22	523	526
		18.7	4.86E-20	4.56E-22	476	483
		10.5	2.06E-21	1.51E-22	500	337
22	RK69	12.8	1.03E-19	6.76E-22	498	486
		15.6	9.74E-21	1.44E-22	486	483
		18.7	5.66E-20	3.38E-22	493	451
		10.5	8.41E-22	1.89E-22	582	226
23	deV52+RK70	12.8	3.32E-20	2.97E-22	467	534
		15.6	4.18E-21	2.22E-22	516	545
		18.7	1.54E-20	3.84E-22	477	498
		10.5	9.80E-22	1.44E-22	352	421
		12.8	7.08E-20	8.77E-22	487	518

Table 2—Continued

Order	Source	Line μm	Flux W cm ⁻²	1 σ error W cm ⁻²	FWHM km s ⁻¹	V _r km s ⁻¹
24	RK20	15.6	7.03E-21	2.78E-22	541	555
		18.7	3.61E-20	3.64E-22	496	489
		10.5	6.61E-22	1.60E-22	328	371
		12.8	1.78E-20	4.29E-22	485	512
		15.6	3.87E-21	3.19E-22	580	538
		18.7	7.85E-21	4.53E-22	450	499

Table 3. Derived Parameters for the H II Regions in M83

Order	Source	R_G kpc	$\frac{Ne^+}{S^{++}}$	$\frac{Ne^{++}}{S^{++}}$	$\frac{Ne^{++}}{Ne^+}$	$\frac{S^{3+}}{S^{++}}$	$\frac{Ne}{S}$	$\frac{>}{$	$\frac{>}{>}$	$\frac{>}{>}$
1	RK275	5.16	23.4 ± 0.3	1.49 ± 0.05	0.0635 ± 0.0023	0.0143 ± 0.0018	24.6 ± 0.3	0.610 ± 0.008	0.104 ± 0.004	7.26 ± 0.92
2	RK268	4.51	25.4 ± 1.4	3.10 ± 0.17	0.122 ± 0.007	0.101 ± 0.019	25.8 ± 1.0	0.564 ± 0.031	0.217 ± 0.012	2.15 ± 0.41
3	RK266	4.29	22.9 ± 0.5	1.98 ± 0.23	0.0865 ± 0.0098	0.0199 ± 0.0052	24.4 ± 0.5	0.623 ± 0.015	0.139 ± 0.016	6.96 ± 1.96
4	RK230	2.50	25.7 ± 0.9	2.88 ± 0.16	0.112 ± 0.005	0.0180 ± 0.0028	28.1 ± 0.9	0.556 ± 0.020	0.202 ± 0.011	11.2 ± 1.8
5	deV10	2.34	28.7 ± 1.0	1.55 ± 0.18	0.0540 ± 0.0061	0.0105 ± 0.0007	29.9 ± 1.0	0.498 ± 0.016	0.108 ± 0.013	10.3 ± 1.3
6	RK213	2.07	27.9 ± 0.2	0.813 ± 0.039	0.0292 ± 0.0014	0.00343 ± 0.00057	28.6 ± 0.2	0.513 ± 0.004	0.0569 ± 0.0028	16.6 ± 2.9
7	deV13	2.15	28.2 ± 0.3	1.32 ± 0.11	0.0469 ± 0.0038	0.00818 ± 0.00109	29.3 ± 0.3	0.506 ± 0.006	0.0925 ± 0.0076	11.3 ± 1.8
8	RK211	2.23	25.4 ± 1.0	1.13 ± 0.07	0.0446 ± 0.0022	0.00820 ± 0.00086	26.3 ± 1.0	0.563 ± 0.022	0.0792 ± 0.0048	9.66 ± 1.05
9	RK209	2.02	25.8 ± 0.2	1.31 ± 0.03	0.0507 ± 0.0013	0.00630 ± 0.00071	27.0 ± 0.2	0.553 ± 0.005	0.0917 ± 0.0023	14.6 ± 1.7
10	RK201	4.00	26.4 ± 2.5	2.39 ± 0.32	0.0907 ± 0.0089	0.0376 ± 0.0067	27.7 ± 2.6	0.542 ± 0.052	0.167 ± 0.023	4.45 ± 0.79
11	RK198	2.18	23.1 ± 0.5	1.70 ± 0.05	0.0733 ± 0.0021	0.0155 ± 0.0018	24.5 ± 0.4	0.618 ± 0.013	0.119 ± 0.004	7.64 ± 0.90
12	deV22	1.91	31.4 ± 0.4	1.21 ± 0.03	0.0387 ± 0.0009	0.00662 ± 0.00105	32.4 ± 0.3	0.456 ± 0.006	0.0849 ± 0.0020	12.8 ± 2.1
13	RK172	0.95	32.1 ± 1.8	2.31 ± 0.38	0.0719 ± 0.0117	0.0216 ± 0.0057	33.7 ± 1.6	0.445 ± 0.025	0.162 ± 0.027	7.49 ± 2.27
14	RK154	4.41	22.9 ± 0.8	2.27 ± 0.14	0.0992 ± 0.0053	0.0198 ± 0.0030	24.7 ± 0.8	0.623 ± 0.021	0.159 ± 0.009	8.05 ± 1.25
15	deV28	0.77	32.5 ± 1.5	2.05 ± 0.25	0.0630 ± 0.0074	0.0172 ± 0.0050	34.0 ± 1.5	0.439 ± 0.021	0.143 ± 0.018	8.35 ± 2.60
16	deV31	0.46	40.8 ± 0.4	1.33 ± 0.06	0.0326 ± 0.0016	0.00525 ± 0.00041	41.9 ± 0.3	0.350 ± 0.003	0.0931 ± 0.0045	17.7 ± 1.6
17	RK137	0.57	28.4 ± 0.3	0.943 ± 0.043	0.0332 ± 0.0015	0.00366 ± 0.00086	29.3 ± 0.2	0.503 ± 0.005	0.0660 ± 0.0030	18.0 ± 4.3
18	RK135	4.05	25.1 ± 2.1	0.898 ± 0.127	0.0357 ± 0.0047	0.0116 ± 0.0019	25.7 ± 1.8	0.568 ± 0.046	0.0629 ± 0.0089	5.43 ± 1.05
19	RK120	2.48	26.3 ± 0.3	1.39 ± 0.04	0.0528 ± 0.0014	0.0131 ± 0.0006	27.3 ± 0.3	0.543 ± 0.006	0.0973 ± 0.0026	7.43 ± 0.37
20	RK110	1.38	34.9 ± 0.4	1.33 ± 0.06	0.0381 ± 0.0016	0.00624 ± 0.00132	36.0 ± 0.3	0.409 ± 0.005	0.0931 ± 0.0039	14.9 ± 3.2
21	RK86	2.93	27.3 ± 0.2	1.13 ± 0.02	0.0413 ± 0.0007	0.00774 ± 0.00057	28.3 ± 0.2	0.523 ± 0.005	0.0791 ± 0.0013	10.2 ± 0.8
22	RK69	1.89	32.5 ± 0.8	1.78 ± 0.10	0.0550 ± 0.0030	0.0116 ± 0.0026	33.8 ± 0.8	0.440 ± 0.011	0.125 ± 0.007	10.8 ± 2.5
23	deV52+RK70	1.92	29.4 ± 0.5	1.28 ± 0.05	0.0434 ± 0.0018	0.00576 ± 0.00085	30.5 ± 0.3	0.486 ± 0.008	0.0894 ± 0.0036	15.5 ± 2.4
24	RK20	4.28	34.0 ± 2.1	3.23 ± 0.32	0.0950 ± 0.0082	0.0179 ± 0.0044	36.6 ± 2.1	0.420 ± 0.026	0.226 ± 0.023	12.7 ± 3.2